Appendix C

Comparison with Mkn 501 and Conclusion

In this final chapter I wish to discuss the measurement results of the large γ-flares of Mkn 421 in 2001 and how the results fit into the global picture of jet emission. I will compare the observational properties of Mkn 421 with the properties of another AGN, Mkn 501, in order to obtain a clearer picture of jet emission. Mkn 501 has become quite famous in TeV-γ-Astronomy. It was the second AGN which emits γ-rays that has been discovered [Qui96] after Mkn 421. It is of virtually the same distance as Mkn 421 and is therefore very interesting for purposes of comparison. It behaves very similar to Mkn 421 but it has longer variability time scales and a different spectrum [Kra01].

This chapter is divided into two parts. In the first part, ***spectral properties*** of the jet emission are discussed. In the second part, ***time scales and correlations*** between x-ray and γ-ray emissions are presented.

C.1 Spectral properties of γ-flares

The spectra of Mkn 421 and Mkn 501 exhibit some ***quite similar*** characteristics. Both of them are strongly curved and show a cutoff. On the other hand, the spectrum of Mkn 501 exhibits an ***cutoff at higher energies*** than Mkn 421. The best average (over all flare states) spectrum fit of Mkn 501 is [Kra01]:

$$\frac{dF}{dE} = (10.1 \pm 1.2)\, 10^{-11} \left(\frac{E}{1\,TeV}\right)^{-2.0\pm0.19} e^{-\frac{E}{(6.1\pm1.2)\,TeV}} TeV^{-1} cm^{-2} s^{-1} \quad \text{(C.1)}$$

while for Mkn 421 it is [TW]:

$$\frac{dF}{dE} = (7.0 \pm 0.4)\, 10^{-11} \left(\frac{E}{1\,TeV}\right)^{-1.88\pm0.15} e^{-\frac{E}{(3.1\pm0.5)\,TeV}} TeV^{-1} cm^{-2} s^{-1} \quad \text{(C.2)}$$

Tab. C.1 shows the most important spectral parameters in an overview. Measurements in the x-ray region by ASCA and RXTE [Kat01] show that the synchrotron (luminosity) peak of Mkn 421 changes its ***position*** only slightly ***from 0.5 keV*** in the quiescent state ***to 2.0 keV*** in high flare state (see Figures C.1a) and C.2). For the case of Mkn 501 the position changes ***two orders of magnitude***, from ***1.0 keV*** to ***100 keV*** (see Figures C.1b) and C.2). Fig. C.2 shows a measurement of the synchrotron peak position in the x-ray region as a function of the luminosity.

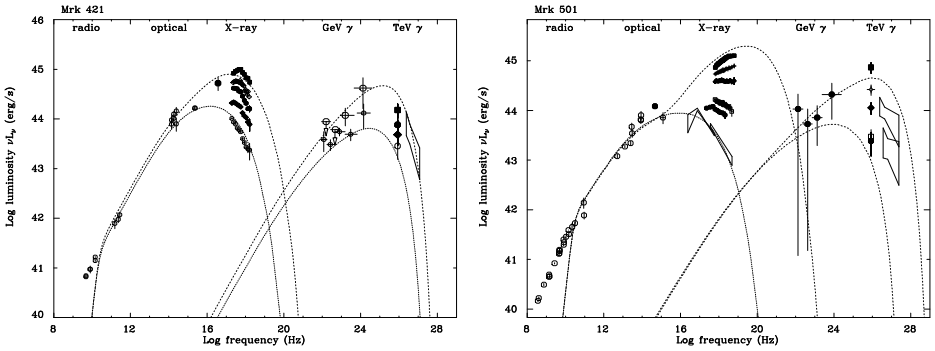

(a) Mkn 421 (b) Mkn 501

Figure C.1: Plots a) and b) show the spectrum of AGN Mkn 421 and Mkn 501, respectively, over the complete frequency range from radio to TeV for various flare states. The dotted line represents the best fit SSC model for the quiescent/flare state. It can be seen that in the case of Mkn 501 the synchrotron peak shifts two orders of magnitude from 1.0 keV to 100 keV, while for Mkn 421 the position changes only slightly from 0.5 keV in the quiescent state to 2.0 keV in high flare state. Taken from [Kat01].

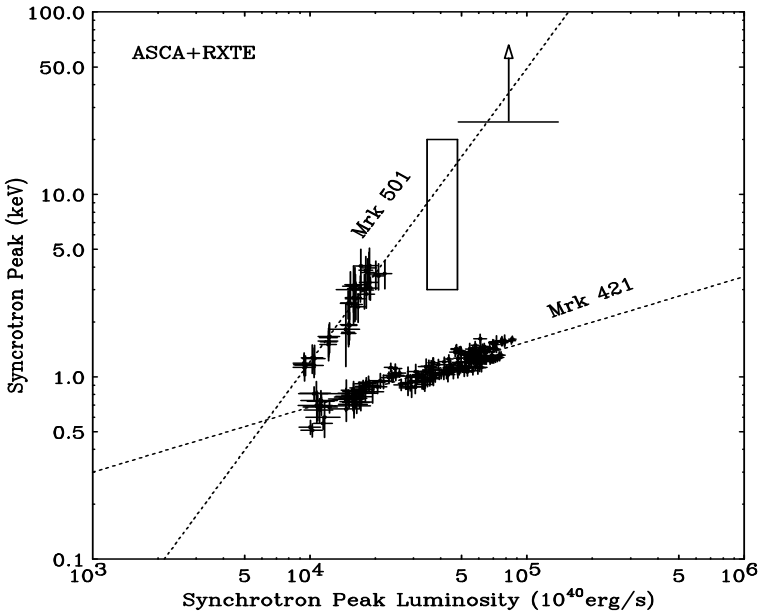

Figure C.2: This figure shows the synchrotron peak position vs. synchrotron peak luminosity for the objects Mkn 421 and Mkn 501 . For the case of Mkn 501 the peak position of the luminosity in relation to the luminosity itself at that point changes much more than for the case of Mkn 421. There the luminosity at peak changes by one order of magnitude while the peak position itself only changes slightly. Taken from [Kat01].

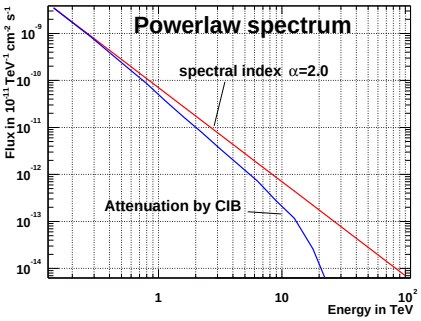

(a) a) Attenuation of high energy gammas

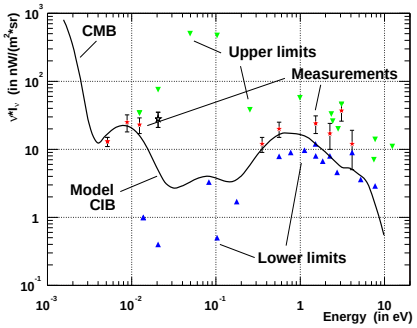

(b) Newst model T. Kneiske and K. Mannheim

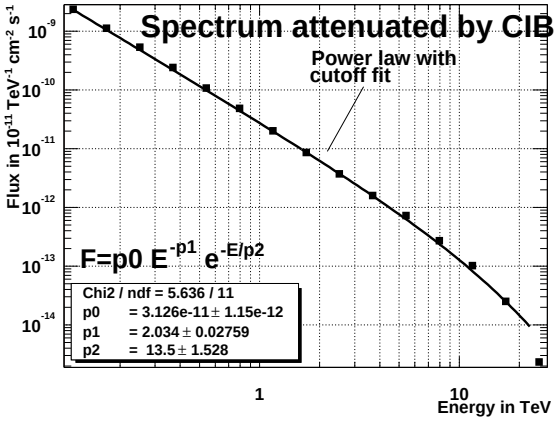

(c) Fit to the attenuated spectrum

Figure C.3: Plot a) shows the effect of the cosmic infrared background (CIB) on a power law spectrum with spectral index 2.0 and for a source that is the same distance from earth as Mkn 421. Strong absorption effects that could lead to a cutoff appear mainly above 10 TeV. Plot b) shows the model for the CIB from T. Kneiske and K. Mannheim [Kne02] and is in good agreement with the actual measurements (red points). Green points are upper limits and blue points are lower limits. Plot c) shows a fit to the power law spectrum that has been attenuated by the CIB model. The fit yields an exponential cutoff at 13.5 TeV. The spectrum decreases faster than exponential above 20 TeV which can be seen in the last point which is far below the fit curve.

Parameter	Mkn 421	Mkn 501
Average flux constant F_0	7.0 ± 0.4 [TW]	10.1 ± 1.2 [Kra01]
Spec. index α (with cutoff)	-1.88 ± 0.15[TW]	-2.03 ± 0.19 [Kra01]
Cutoff in TeV	3.1 ± 0.5[TW]	6.0 ± 1.4[Kra01]
Harden. of spec. dur. flare	yes[TW]	yes[Pir01]
Shift of synch. peak in keV	$0.5 - 2.0$ SSC[Kat01]	$1.0 - 100$[Kat01]
Shift of Comp. peak in GeV	$\sim 20 - 200$ [TW], SSC[Kat01]	$10 - 1000$[Kat01, Pir01]

Table C.1: The table lists the spectral properties of Mkn 421 and Mkn 501. For case of Mkn 501 the cutoff is found at higher energies than for Mkn 421. The synchrotron peak of Mkn 501 shifts by two orders of magnitude from low state to high state while the one of Mkn 421 only shifts by a factor of four. The shift of the inverse Compton peak has been guessed by the fit to a SSC model.

This shift in the x-ray range also implies a potential ***shift of the inverse Compton (luminosity) peak*** (in the γ-ray range), which can only be ***estimated*** by a fit to the SSC model [Kat01]. For the case of Mkn 421, it probably shifts from approximately ***20 GeV*** to about ***200 GeV*** while for Mkn 501 it should shift from about ***10 GeV*** up to ***1000 GeV*** [Pir01].

The difference in the average spectrum (i.e. the different ***cutoff***) for the two objects could be explained by the idea that the inverse Compton (luminosity) peak for the case of ***Mkn 501*** shifts to ***higher*** energies than for the case of ***Mkn 421***. A movement of the position of the inverse Compton peak should show up as a ***hardening*** of the spectrum for higher fluxes. This effect has been observed in this work and also by the Whipple telescope [Kre02], which has a much lower energy threshold and by the CAT telescope [Pir01].

Analysis results

As was shown in the last section a ***hardening*** of the spectrum for higher fluxes was observed. Fits with both ***fixed cutoffs and fixed slope*** (-> no change in shape) were ***rejected*** at the 3.8-sigma level, as was a ***pure power*** law fit (rejected with 5.8 sigma). ***Three*** different hypothesis were fitted to the data of five different flux levels. This were

1. a) ***fix-cutoff/free-slope*** hypothesis: By ***fixing the cutoff*** to ***3.3 TeV*** a significant change in the spectral index for increasing fluxes was observed (α decreased from 2.5 to 1.8).

2. b) ***free-cutoff/fix-slope*** hypothesis: By ***fixing the slope*** to α***=2.0*** a significant change of the cutoff was observed (E_c increased from 1.9 TeV to 4.3 TeV).

3. c) A hypothesis of a ***moving*** inverse Compton peak was tested: By fitting a power law with a quadratic term ***(parabolic fit)*** the position of the peak of the parabola shifted significantly from approximately ***15 GeV*** up to ***80 GeV.***

All ***three*** fits gave ***acceptable*** chisquare values.

The parabola is only a ***very rough*** estimate of the true shape of the inverse Compton peak and the values obtained are only demonstrating the compatability with the idea of a moving peak and say nothing about the ***true*** inverse Compton (luminosity) position. The fit of the parabola ***suggests*** that the ***high variability*** of the flux in the region between 500 GeV and 20 TeV (where Cherenkov telescope measure) might ***not only originate*** from a variablity of the (inverse Compton) peak luminosity but also from the ***shift*** of the inverse Compton peak, since the slope of the spectrum in the region between 500 GeV and 20 TeV is ***very steep*** and any movement of the peak immediately results in a ***large change*** in the flux there (See Fig. B.29).

It was ***not possible*** to clearly ***accept*** or ***reject*** any one of these hypothesis. The true behaviour might involve a combination of these effects.

Parameter	Mkn 421	Mkn 501
Correlation x-ray/TeV (1 day bin)	0.74 ± 0.12[TW]	0.76 ± 0.14[Kra01]
$Flux^{b}_{xray} \propto Flux_{\gamma}$: b	1.0 ± 0.2[TW]	1.96 ± 0.07 [Kat01]
Doubling time of flare (TeV)	15 min.[TW]	$\sim 2\,h$[Kra01]
Doubling time of flare (keV)	$\sim 15\,min$[Car99]	$\sim 2\,h$[Kra01]
Average flare duration (TeV)	$1-3\,h$[TW]	$\sim 2\,days$[Kra01]

Table C.2: The table lists the most important properties concerning time scales and correlations for the objects Mkn 421 and Mkn 501.

The question about the cutoff in the spectra of Mkn 421 and Mkn 501

In an attempt to clarify the ***origin of the cutoff***, one could start examining the effects of the CIB (Fig. C.3). The question is whether the cutoff is an ***intrinsic*** feature of the real emission spectrum or a result of the ***absorption*** of γ-rays due to the cosmic infrared background (gamma ray horizon). In Fig. C.3a), the ***effect*** of the CIB absorption on a power law spectrum of α=2.0 is displayed. The model used for the CIB is [Kne02] that fits the actual CIB measurements very well. Due to the ***steepness*** of the spectrum, a true ***cutoff effect*** can only be observed ***above 10 TeV.*** A fit to the attenuated power law spectrum yields an exponential ***cutoff at 13.5 TeV*** while it has to be kept in mind that the attenuation above 10 TeV is much stronger than exponential. This suggests that the ***dominant*** reason of observed cutoff in the spectra of both Mkn 421 and also of Mkn 501 might favor the hypothesis of an intrinsic cutoff (***increasing cutoff energy with increasing flux***) and a ***moving inverse Compton peak***.

C.1.1 Time scales, correlations and jet models

Time scales of flares and correlations between x-ray emission and γ-ray emission also provide us with hints of the physical mechanisms inside the jets. Tab. C.2 provides an overview of the most important parameters.

Correlation of x-ray emission and γ-ray emission

Both sources show a ***strong correlation*** between the x-ray flux and the γ-ray flux. For Mkn 421, a correlation coefficient of 0.74 ± 0.12 (this analysis, one day bins) and for Mkn 501, a correlation coefficient of 0.76 ± 0.12 [Kra01] was observed. This correlation provides hints about the mechanism of γ-ray production. Today it is widely assumed that high energy gammas are produced via inverse Compton up-scattering of soft photons. The question is whether the soft photons emerge from the ***accretion disc*** or whether they are produced ***inside*** the jet. The high correlation can only be explained if both production mechanisms are ***coupled*** and very close to each other in distance. If the soft photons (i.e. x-ray photons) would originate from the accretion disc then the correlation would be ***zero*** or even ***negative*** (x-ray dip). This means that an existing correlation clearly ***favors*** a SSC model and as a consequence, potential quasi-periodicities (like the 23 +- 2 day periodicity of Mkn 501 [Kra01]) ***cannot*** be explained by a ***modulation*** of soft photons ***emerging from the accretion disc*** [Bed96]. Quasi-periodicities should be explained by other models like helical jets, periodic ejection of the jet by a big rotating object close to the innermost stable orbit of the (Kerr-) black hole [Mas99] or binary black holes [Beg80, Man00].

The ASCA x-ray measurement

Interesting results are obtained from the ASCA-x-ray/γ-ray correlation study that also shows a ***strong correlation*** between x-ray flux (ASCA measurement from April 1998) and the γ-ray flux. In addition, we divided the x-ray flux into a ***slow flare*** component

(of several days duration) and a ***fast component*** (of a few hour duration). It appears that the correlation between x-ray and γ-ray ***increases*** from 0.63 +- 0.18 to 0.70 +- 0.16 when the slow x-ray component (the background) is subtracted. However, the increase is not significant and does not allow further conclusions.

Relation between the x-ray flux and γ-ray flux

In the case of ***Mkn 501*** the x-ray/γ-ray relation is ***quadratic*** ($Flux_{xray} \propto Flux_{Gamma}^{1.96\pm0.07}$ [Aha99/2]) while for ***Mkn 421*** it is ***linear*** ($Flux_{xray} \propto Flux_{Gamma}^{1.0\pm0.2}$) (see the previous chapter). The latter measurement is in agreement with [Aha99/1] and is also confirmed by the ***ASCA-x-ray/γ-ray*** correlation study (see the previous chapter). This difference between the objects can be explained by the fact that the peak position (of the inverse Compton peak) of Mkn 501 shifts ***much stronger*** with changes in its luminosity.

The argument is the following. The change in flux that we observe in the small TeV window might not only originate from a ***real increase*** in the luminosity (at peak) but also from a ***movement*** of the inverse Compton peak. Since the movement for the case Mkn 501 is presumed to be ***larger***, the change in ***flux*** in the 500 GeV to 20 TeV window is expected ***much larger*** (it is ***quadratic***) in contrast to Mkn 421 in which case the change in ***flux*** (in the TeV window) should be ***less*** (since the inverse Compton peak is ***moving less*** it is ***linear***). This means that the difference in the relation between x-ray fluxes and γ-ray fluxes is strongly related to the ***question*** at which ***positions*** we find the synchrotron/inverse Compton peaks, which ***shape*** they have and in which ***energy intervals*** we measure the flux.

In the future, more precise multiwavelength measurements will provide the possibility to reject or accept different SSC model theories.

Observable and intrinsic parameters of the classic SSC model

The simplest SSC model (assuming only a single ***spherical emission region***) was presented in the introduction chapter (in detail in Appendix A) and has the following seven independent parameters: The normalization constant K, the energy break energy γ_b, the radius of the emission region R, the magnetic field B, the Doppler factor δ and the positions of the peak luminosities of the synchrotron radiation ν_s and of the inverse Compton radiation ν_C [Ino96].

The spectral observations in the x-ray and the γ-ray energy region are the ***shape*** of the spectra, the two peak ***luminosities***, the ***variability time scales*** and a potential ***time lag*** between the x-rays and the γ-rays. The structure of the equations allows to express strong constraints on B and δ [Tav98]. For the case of Mkn 421, using the single emission region model and a variability with a ***very conservative*** time scale of $t_{var} = 1\,h$, the magnetic field B and the Doppler factor δ result in $B \simeq 0.25$ Gauss and $\delta \simeq 25$. This ***atypical high*** Lorentz factor is meant to provide an explanation for the ***very rapid*** variability time scales observed.

Variability t_{var} and the size of the emission region R

The time scales of the flares are quite different for the two sources. Mkn 421 shows ***doubling times*** of equal to or faster than ***15 minutes*** (see the analysis of the previous chapter) while Mkn 501 has doubling times of about 2 hours [Kra01]. The typical (fast) flare duration (FWHM) for Mkn 421 is approximately 1-3 hours [TW] while for Mkn 501 it is about 2 days .

These variabilities can be explained by varying the ***dimensions*** of the emission regions of the jets of these objects and by ***different Doppler factors*** due to varying bulk jet ***Lorentz factors***.

For the case of Mkn 421, for reasons of causality, the small variability time scale of $t_{var} = 15$ minutes puts ***hard constraints*** on the ***size*** of the emission region and/or on the Doppler factor δ:

$$R \leq c t_{var} \delta \tag{C.3}$$

This implied that for Mkn 421, assuming a ***typical*** Lorentz factor of $\delta = 10$ (which cannot be much higher for Blazars as explained in the introduction chapter), that the emission region must be ***very small***, less than $R = 2\,10^{12}\,m \simeq 10\,AU \simeq 10^{-4}\,pc$. Typical jet scales are approximately $0.01 - 0.03\,pc$. Jet dimensions are ***strongly constrained*** by the ***transparency or photon-photon opacity condition*** which sets lower limits [Mas99] on them. Therefore jet scales with sizes of order $10^{-4}\,pc$ are ***virtually ruled out*** for the observed ***luminosity***.

The ***other possibility*** for this model is to ***increase*** the Lorentz factor up to values of δ=80. This scenario is ***unrealistic***, especially since it is known that the (cooled) radio blobs (the superluminal motion is only 2-3) of these objects are ***slower*** than those of typical blazars and radio galaxies.

Shock-in-jet models

Obviously the standard jet model of a spherical emission region ***seriously breaks down*** when it attempts to explain the ***very short variability time scales***. For this reason, new models have been developed which are able to explain the fast variabilities ***without*** increasing the Doppler factor. All of them introduce ***moving laminar shock fronts*** inside the jet instead of a spherical emission region. Thin ***'sheets'*** of shock fronts move inside the jet towards the observer. Typical source dimensions have ***radii*** of approximately $R = 10^{14}\,m \sim 0.01\,pc$ and ***thicknesses*** of $d = 7 \cdot 10^{11}\,m \sim 5 \cdot 10^{-5}\,pc$. These so-called ***shock-in-jet*** models provide a natural explanation for very short variabilities [Mas99] (a more detailed discussion can be found in [Sal98]).

When looking at the recorded flares of Mkn 421 (intra day variability, lightcurves for each night) one gets the impression that a ***large flare*** (several days duration) is mainly a ***superposition*** of many ***small flares.*** This image was used as a ***basis*** for the flare model that was fitted to the intraday lightcurves (last chapter, fitting of flare times): The flux of a single flare is $F(t) = a + \frac{b}{\left(2^{(t-t_0)/c} + 2^{-(t-t_0)/d}\right)}$. In this model a ***constant background*** 'a' (the pile-up of many flares), an ***exponential rise time*** 'c' (the acceleration inside laminar shocks-in-jet) and an ***exponential cooling time*** 'd' (the cooling via synchrotron radiation and inverse Compton scattering) was assumed. This picture naturally emerges from shock-in-jet models because there one expects many shocks in ***parallel*** which cross the jet at the same time.

In addition, the measurements of ***ASCA*** in the x-ray energy region (last chapter, correlation measurements between x-rays and γ-rays) seem to show a ***slow flare*** component and ***fast overlapping*** flares. The slow component covering several (about seven) days refers to the ***emerging of a blob*** and the fast short flares refer to the ***shocks-in-jet*** that traverse the blob. This would explain why the correlation seems to increase if the slow component (in the x-ray) is subtracted from the total before calculating the correlation.

Potential timelag of the x-rays

In the analysis of the Mkn 421 flares in 2001 we have observed a hint that the x-rays may be ***delayed*** with respect to γ-rays by approximately ***10 hours.***

The ***observed timelag*** of the x-rays had only an estimated significance of ***three sigma*** since the mentioned systematical error is large. However, a potential timelag can originate from four possible situations:

1. ***Asymmetric x-ray flare shape:*** A significantly ***shorter rise time*** than ***fall time*** of the x-ray flares could result in an effect as seen in the last chapter. The resulting shape of the discrete correlation function would also be ***asymmetric*** [Bad98, Jor01] and the observed effect thus cannot be interpreted as a ***physical*** timelag. This means that a non-linear and complicated ***transfer function*** of the ***x-ray*** flux to γ-***flux*** could result in an ***asymmetry*** of the discrete correlation function around zero time lag. Unfortunately, the ASM data does not allow to give answers about the shape of x-rays flares and the transfer function.

2. ***Opacity effects:*** Different ***optical opacities*** of the jet for x-rays and γ-rays can have the effect that x-rays arrive later. The x-rays are ***trapped*** and scattered inside the jet and can only escape the jet when it is sufficiently cooled down whereas the γ's ***escape immediately*** [MagCom].

3. ***Cooling effects:*** Another explanation could involve ***cooling*** of the high energy electrons. The $e^{\pm}$in the jet are cooled down via synchrotron radiation and inverse Compton scattering. A natural consequence of electron cooling is a ***time lag*** of soft x-rays with respect to hard x-rays. The argument is the following: In high state the x-ray spectrum is ***hard*** and becomes ***softer*** as it cools down. The more energetic x-rays ***appear first*** and later (after cooling) ***soft x-rays dominate*** the spectrum. This introduces the time lag. Since the inverse Compton peak is sort of ***mirror*** of the synchrotron peak, a time lag between soft x-ray and γ-rays is also observed. The estimated order of magnitude of the time lag between soft and hard x-rays is (i.e. the decay time of electron energy) is given by [Dar97]:

$$t_{lag} \sim 10^3 \frac{H_{\perp}^{-3/2}}{Gauss} \frac{E_{\gamma}^{-1/2}}{keV} \delta^{-1/2} \sim \ a\ few\ hours \tag{C.4}$$

   H is the magnetic field in Gauss, E_{γ} id the energy of the electron in keV and δ is the Lorentz factor. ***Common*** electronic jet models [Dar97](with a spherical emission region) have ***difficulties*** to explain the fast cooling times of electrons that are at the same time ***efficiently accelerated*** to ultra high (TeV ranges) energies. Shock-in-jet models ***avoid*** these problems because acceleration and cooling are separated and happen at ***different*** positions in the jet [Sal98]. It should be mentioned that short fall times that have been measured for γ-ray flares don't imply that x-ray flares also have short fall times (cooling). It is probable that x-ray flares have a different shape than γ-flares.

4. ***Quantum gravity:*** The timelag could be a ***first sign of quantum gravity*** effects where theoreticians expect changes in the ***speed of light*** for photons with energies close to the Planck mass. The time lag of x-rays would point to an ***increase*** of the speed of light for increasing photon energies [Ame00, Ame96]. Even that the energy of TeV photons is far away from the Planck scale, the long distance from Mkn 421 to earth could help to amplify even tiny effects.

As a conclusion we can only give an upper limit on the time lag of about 13 ± 3 hours.

Future multiwavelength observations with advanced instruments will clarify these questions in greater detail. Larger, future Cherenkov telescopes record with higher statistics and will provide the possibility to find time lags within GeV/TeV data only.

Fast variability and the mass of the black hole

The variability time scale is approximately 15 to 20 minutes. The appearance of the fast flares is ***entirely random***. Therefore, they are not a result of helical jets or objects close to the innermost stable orbit of the black hole but rather an effect of the jet dynamics itself. A very plausible explanation for this are the ***laminar shock fronts*** inside the jets, which was

just discussed. The jet has ***not a direct*** relation to the size of the central black hole. This implies that an estimate of the mass of the black hole ***cannot*** be found here.

Generally, it is assumed that the nucleus of Mkn 501 has a mass of 10^8 solar masses. Mkn 421 is considered to be smaller than Mkn 501 by 2 orders of magnitude, with an estimated mass of 5×10^6 solar masses because of the shorter variability. The mass of the black hole is generally presumed to scale with $m \propto t_{var}$ because the circling time around the black hole scales linearly with mass.

C.2 Outlook

Future Cherenkov telescopes as MAGIC on the island of La Palma, HESS in Namibia or VERITAS have ***lower energy thresholds***, ***higher sensitivities*** and much ***higher effective detection areas.*** They record with a much higher event rate and achieve ***better statistics*** and a ***better separability*** of γs and hadrons. It will be possible to clarify to a higher level the following questions which have been touched in this work:

1. It might be possible to directly observe the ***energy of the peak luminosity*** with lower energy thresholds or at least to give precise estimates by fitting the SSC model. It will be for sure possible to significantly clarify the question whether ***peak moves*** with varying luminosity or not. This gives an answer to the question of the ***origin of the cutoff***.

2. Preciser data might allow to see if the observed spectrum contains ***contributions of gamma photons from π^0-decay*** and will therefore detect ***hadronic components*** in the jet and confirm whether the jet is purely electronic or not. Neutrino experiments like Amanda and Ice Cube at the South Pole and Antares in the Mediteranian Sea will help answering the question about hadronic contributions in jets (the detection of neutrinos prove the existence of hadrons). The detection of hadrons would help to solve one of the most urgent questions in cosmic ray physics: Where do the high energy hadrons come from ?

3. Since the threshold of the new instruments is ***lower, more objects*** behind the actual gamma ray horizon will be seen. This gives information about the ***exact position*** of the gamma ray horizon and therefore about the ***evolution of star formation*** during the history of the universe (cosmic infrared background) and also about cosmic parameters as for example the ***cosmological constant*** [Bla01]. The determination of the position of the gamma ray horizon will also clarify the ***origin of the cutoff*** in the spectra.

4. Measurements over two to three orders of magnitude of the high energy scale (30 GeV to 30 TeV) with high statistics will open the possibility to detect ***possible time lags*** of fluxes in lower energy regions (<100 GeV) to fluxes in higher energy regions (>1 TeV) ***within the same γ-ray dataset*** only.

5. With higher statistics ***rise times*** (acceleration) and ***fall times*** (cooling) of the flares can be measured in a more accurate way. It will be possible to observe whether long flares are a ***superposition*** of ***many small flares*** or if other components come into play. This will gives us a better understanding of the jet model and the mechanisms that are active in jets.

Simultaneous multiwavelength campaigns with precise x-ray measurements are mandatory for the following reasons:

1. It will be possible to determine the exact ***transfer function*** of x-ray flux to γ-flux, the acceleration time and the cooling time of the high energy particles in the jet.

This will tell us which processes take place in jets, whether there are ***laminal shock fronts*** or not and how γ-rays are produced.

2. When the transfer function is known, the question about the ***time lag*** of x-rays to γ-rays will be solved in a more accurate way. It might be possible to detect signals of quantum gravitation.

Appendix D

Summary

Today astroparticle Physics is one of the most booming fields in modern physics. Gamma ray astronomy is a ***major tool*** to analyze and understand the ***origin*** of cosmic rays. The BL LAC object, ***Mkn 421***, belongs to a class of objects that ***emits*** cosmic rays, the so-called ***active galactic nuclei*** (AGN). In a stochastic but regular manner it switches from a ***quiescent*** state to a state of ***high activity*** in which it starts to emit photons in the x-ray and TeV energy range. From ***February 2001 until April 2001*** it exhibited especially large and long ***flares,*** which have been observed by many telescopes in the TeV energy range as well as by the CT1 telescope of the HEGRA collaboration at La Palma and in the x-ray energy range by the ***All Sky Monitor*** (ASM) of the RXTE satellite. Another flare happened in April ***1998*** which has been observed by the ***ASCA*** x-ray satellite and simultaneously by ***several*** Cherenkov telescopes including ***Wipple***. I present here an analysis of the la***rge gamma flares of 2001*** and also of the short flare in April 1998.

The ***classical*** analysis and gamma/hadron separation methods of Cherenkov telescopes have been improved by several ***new techniques***, which have been tried and tested for the first time here. A complete analysis package of approximately 50.000 lines of code has been developed in ***ROOT/C++*** which contains, apart from the items of a standard analysis for Cherenkov telescopes, the following ***new features:***

- A ***modified linear discriminant analysis*** to enhance the ***gamma/hadron separation***. It is also used as a tool to ***quantify*** the separation capability of different ***sets*** of (new) image parameters and new image cleaning algorithms that have been tested and studied in detail.

- Different algorithms that perform so-called ***image cleaning,*** a technique which is widely used to remove noise background in the image, have been tried and tested with respect to ***improvement*** of ***gamma/hadron separation.***

- Introduction of ***new*** image parameters that improve ***gamma/hadron separation*** and the

- Introduction of ***weights*** in the calculation of the ***image parameters***, the so-called ***'Hillas'*** parameters, which improve ***gamma/hadron separation***

- A systematic algorithm that tests virtually all possible combinations of parameters and image cleaning to find the one with optimal ***gamma/hadron separation.***

- A new method to correct the ***mispointing*** of the telescope. This ensures zenith angle independent integrated flux measurements.

- Unlike the ***usual*** case, the characteristic parameters and features of the emission spectrum have not only been deduced from the ***unfolded flux spectrum*** but rather,

vice-versa, by fitting ***raw excess event energy distribution.*** In this way an unsatisfactory and potentially unreliable ***unfolding process*** is avoided and the fit results (i.e. the spectrum parameters) have less errors and are more robust.

In addition to these improvements, the ***standard items*** have also been implemented. They are:

- A program to ***estimate the energy*** on the basis of the ***least squares*** method. It achieves an average energy resolution of approximately 24 %.
- A program to calculate ***effective areas.***
- A program to calculate the ***spectrum*** by ***unfolding*** the ***energy resolution*** obtained from MC generators. This not only solves the ***spill-over*** problem from higher energy bins to lower energy bins, but it also corrects for systematic biases introduced by an energy estimate that is ***not*** completely ***linear.***
- A program to calculate the time dependent integrated flux (***light curve***) in various energy ranges. The According effective areas have been determined from the actual shape of the spectrum, which was previously calculated.
- A program to calculate the ***hardness ratio*** of the lightcurve.
- A program to calculate the ***correlation*** between x-ray lightcurves and γ-ray lightcurves.
- A program that ***simulates the night sky background*** in the MC gamma data sample.

The improved analysis has been ***applied*** to the measurements of the ***large gamma flares*** in 2001 of Mkn 421. 249 hours of observation time have been accumulated, which allows several detailed studies with good statistics:

- A detailed lightcurve with 20 minute bin size granularity, which reveals the extremely ***fast flares*** of this object. The minimal doubling and halving times and the typical FWHM duration of fast flares were estimated.
- The flux dependence of the ***hardness ratio*** was examined for different energy intervals. Evidence of a change in spectral index below 2 TeV from low to high fluxes has been observed.
- The ***correlation*** between the γ-TeV-flux and the x-ray light flux as measured by the ASM/RXTE (0.5 keV to 10 keV) has been calculated.
- The ***average spectrum*** and it characteristics have been calculated and determined.
- The ***spectral behaviour*** of the source during ***different flare states*** has been carefully analyzed in order to see if the effect observed, using the hardness ratio, could also have been observed directly from the spectrum.

In brief, the ***final results*** are the following:

- The spectrum of the Crab nebula was calculated and yielded a pure powerlaw with a spectral index of $\alpha = 2.5 \pm 0.1 \pm 0.1$ and a flux constant of $F_0 = 3.0 \pm 0.33 \pm 0.5\ TeV^{-1}cm^{-2}s^{-1}$ which is in good agreement with the measurements of other Cherenkov telescopes.
- A pure power law fit to the averaged spectrum of Mkn 421 was ***rejected*** by a chisquare of χ^2/NDF=74/9. A ***power law fit with exponential cutoff*** was accepted by a chisquare of χ^2/NDF=6.3/8. The spectral index is $\alpha = 1.88 \pm 0.15 \pm 0.1$. The cutoff was found at $E_c = 3.1 \pm 0.5 \pm 1.0$ TeV.

- The spectrum for ***five different flux levels*** were calculated and it was possible to show that the spectrum changes significantly with increasing flux: It gets ***harder.*** The hardening of the spectrum in the region below 2 TeV could be ***verified*** by an independent analysis using the hardness ratio.
- ***Three*** different hypothesis were fitted to the five spectra. For statistical reasons only functions with ***two free*** parameters were used. All three hypothesis yielded ***acceptable*** chisquare values. The hypothesis were:
  - A power law hypothesis with ***fixed cutoff*** at $E_c = 3.2\,TeV$ and free slope: The spectral index ***decreased*** significantly with increasing flux (a fixed spectral index with fixed cutoff was rejected at the 3.8 sigma level).
  - A power law hypothesis with ***fixed slope*** $\alpha = 2.0$ and free cutoff: The cutoff ***moved*** significantly from 1.9 TeV up to 4.3 TeV.
  - A power law with a ***parabolic (quadratic)*** term: The peak (luminosity) of the parabola ***moved*** significantly from 13 TeV up to 78 TeV (a fixed parabola peak was rejected at the 3.5 sigma level) indicating that the change of the spectrum is ***compatible*** with a ***moving*** inverse Compton peak. The peak of the parabola is only a ***very rough estimate*** of the real luminosity peak. Still, the ***movement*** was ***significant.***
- The TeV lightcurve has been examined at ***single night*** basis. The rise and fall time were estimated in ***three*** independent different manners.
  - A fit of a simple flare model allowed to determine some flare parameters as ***rise time***, ***fall time*** and ***average duration*** (FWHM). The model assumes a ***constant background*** and ***exponential*** rise and fall times. The ***average short flare duration*** (FWHM) is of the order of ***1 to 3 hours.*** The model shows that most of the fast flares have ***doubling rise times*** and ***halving fall times*** of about ***25 minutes***. No significant ***difference*** between rise and fall times could be found.
  - The doubling rise time and halving fall time were calculated by using a ***4-point/three-straight-line*** fit. The fit values show that the fastest flares have doubling times of ***at most 15 to 25 minutes.***
  - The doubling rise time and halving fall time were calculated by only measuring the rise and fall between ***two points.*** Since this method is ***sensitive*** to fluctuations in the flux data points and therefore can result in ***underestimated*** rise/fall times, the slope of the straight line connection between the two points was calculated by ***subtracting/adding*** one sigma on each beforehand (***worst case scenario***). The fastest flares showed rise and fall times of ***at most 15 minutes.***
- The x-ray flux measured with ASM/RXTE shows a ***clear and significant correlation*** to the TeV data of approximately ***0.74+-0.12*** (for one day bins).
- Both correlation studies, with CT1/ASM data and ASCA/TeV data, yielded a ***linear relation*** between x-ray flux and γ-ray flux.
- A hint of a ***potential time lag*** (about 10 h+-2 h) of the x-rays to the γ-rays showed up. It appears that the hypothesis of a x-ray time lag of several hours compared to γ-rays could ***not*** be ***significantly*** proven because of the uncertainty in the ***estimation of the systematic error***. However, every correlation curve shows a systematic time lag for the complete range of time-bin widths, from 1 day down to 0.5 h. The apparent time lag could be a result of an ***asymmetric shape*** of the x-ray flares with a short rise time and a very long fall time. Therefore only an ***upper limit*** on the time lag of 13 ± 3 hours is given here.

- A flare of Mkn 421 in April 1998 as measured by the ASCA x-ray satellite was analyzed and the correlation to γ-ray measurements of several telescopes was calculated. A ***significant correlation*** was found. The x-ray data was splitted into a ***slow flare*** component (seven days duration) and a ***fast*** flare component (several hour duration). The correlation of the TeV flux to the total x-ray flux was ***0.63+-0.18*** and increased to ***0.70+-0.16*** when the ***slow*** component was ***subtracted*** from the lightcurve. The increase is not significant enough to give further conclusions.

Appendix E

Appendix A: Theory and calculations

E.1 Verification of the NSB distribution function

In the introduction chapter the ***excess noise factor F*** has been introduced with the following general definition:

$$F^2 = \frac{Signal^2_{input} / \left(\sigma^2_{input} - \sigma^2_{el}\right)}{Signal^2_{output} / \left(\sigma^2_{output} - \sigma^2_{el}\right)} \tag{E.1}$$

The noise at the input and at the output is understood as noise ***without*** electronic noise from the amplifier $\sigma^2_{noise} = \sigma^2_{real} - \sigma^2_{el}$.

The output distribution of a PMT (Gain normalized to Gain=1) when exposed to diffuse night sky background (NSB) has been described as the ***Poisson distributed sum of Gaussian normal distributions***.

$$f_\lambda(x) = \sum_{n=0}^{\infty} \frac{e^{-\lambda}\,\lambda^n}{n!} \frac{e^{-\frac{(x-n)^2}{2\sigma_n^2}}}{\sigma_n\sqrt{2\pi}} \tag{E.2}$$

with a ***variance*** of

$$\sigma_n^2 = \quad n\left(F^2 - 1\right) + \sigma^2_{el} \tag{E.3}$$

λ is the ***average*** amount of photoelectrons that hit the first dynode, ***n*** is the number of photoelectrons, σ_n^2 is the variance of the individual photoelectron peak and σ_0^2 is the ***variance of the pedestal*** which is equal to the ***electronic noise*** contribution $\sigma_0^2 = \sigma^2_{el}$.

Now we want to ***cross check*** if the proposed output distribution (Equ. E.2) is ***consistent*** with the definition of the excess noise factor.

1) We calculate the ***average*** of $f_\lambda(x)$:

$$\langle f_\lambda(x)\rangle = \int_{-\infty}^{+\infty} f_\lambda(x)\; x\, dx \tag{E.4}$$

$$= \int_{-\infty}^{+\infty} \left(\sum_{n=0}^{\infty} \frac{e^{-\lambda}\,\lambda^n}{n!}\, x\, \frac{e^{-\frac{(x-n)^2}{2\sigma_n^2}}}{\sigma_n\sqrt{2\pi}} \right) \tag{E.5}$$

$$= \sum_{n=0}^{\infty} \frac{e^{-\lambda}\,\lambda^n}{n!}\, n$$

$$= \lambda \;\; OK.$$

2) We calculate the ***variance*** of $f_\lambda(x)$:

$$\begin{aligned} var_x\left(f_\lambda(x)\right) &= \left\langle (x-\overline{x})^2 \right\rangle \\ &= \int_{-\infty}^{+\infty} \left(\sum_{n=0}^{\infty} \frac{e^{-\lambda}\lambda^n}{n!} (x-\lambda)^2 \frac{e^{-\frac{(x-n)^2}{2\sigma_n^2}}}{\sigma_n\sqrt{2\pi}} \right) \end{aligned} \tag{E.6}$$

With $(x-\lambda)^2 = (x-n)^2 + 2(n-\lambda)(x-n) + (n-\lambda)^2$ we get

$$\begin{aligned} var_x\left(f_\lambda(x)\right) &= \sum_{n=0}^{\infty} \frac{e^{-\lambda}\lambda^n}{n!} \left\{ \sigma_n^2 + (n-\lambda)^2 \right\} \\ &= \lambda\left(F^2-1\right) + \sigma_{el}^2 + \lambda^2 - 2\lambda^2 + \lambda^2 + \lambda \\ &= \lambda F^2 + \sigma_{el}^2 \end{aligned} \tag{E.7}$$

3) We introduce $Signal_{input} = Signal_{output} = \lambda$, $\sigma_{input}^2 = \lambda$ and $\sigma_{output}^2 = \lambda F^2 + \sigma_{el}^2$ in Equ. E.1:

$$\frac{\left(\lambda/\sqrt{\lambda}\right)^2}{\left(\lambda/\sqrt{\lambda F^2}\right)^2} = F^2 \quad OK. \tag{E.8}$$

E.2 The synchrotron self Compton (SSC) model

In the SSC model[1] the gamma-ray photons are produced by the inverse Compton scattering of soft photons. These soft photons are generated by the same electrons stemming from the synchrotron emission (see Fig 1.6). The model discussed here has been described in [Ino96, Blo96]. It is based on the following assumptions:

1. A ***spherical emission*** zone which is stationary and has a parameter R that describes all length scales.
2. An ***electron distribution*** $N(\gamma)$ which is parameterized as a ***broken power law*** (K is a normalization constant, α is the spectral index of the shock acceleration (eg. $\alpha = 2.2$), γ is the electron lorentz factor and γ_b is the breaking energy)

$$N(\gamma) = K\gamma^{-\alpha}\left(1 + \frac{\gamma}{\gamma_b}\right)^{-1} \tag{E.9}$$

3. The soft photons[2] needed for the inverse Compton scattering are ***synchrotron photons***.
4. All particle and photon distributions are ***isotropic*** in the jet frame.

The electron spectrum has the shape of a ***broken*** power law because of ***cooling effects*** during the shock acceleration process. The high energy electrons are continously cooled by synchrotron radiation and inverse Compton scattering. The breaking energy results to be

$$\gamma_b = \frac{3mc^2}{4\left(u_b + u_{soft}\right)\sigma_T R} \tag{E.10}$$

with magnetic field density

$$u_B = \frac{B^2}{8\pi} \tag{E.11}$$

The electron energy is given in terms of the Lorentz-factor γ, B is the magnetic field in Gauss, K is a normalization constant, σ_T is the Thompson cross section and m is the mass of the electron in EGS units. γ_b breaks the spectrum by one power in the index.

Synchrotron radiation

The ***basic formulas*** for ***the synchrotron radiation*** are described in the following.

1. ***The spectral density*** is

$$I_\nu = \frac{j_\nu}{\alpha_\nu}\left(1 - e^{-\alpha_\nu R}\right) \tag{E.12}$$

2. where j_ν and α_ν are the ***emission*** and ***absorption coefficient*** for the synchrotron radiation, which are calculated in the following way:

$$j_\nu = c_2 B \int_{\gamma_{min}}^{\gamma_{max}} d\gamma N\left(\gamma\right) F\left(\frac{\nu}{c_1 B\gamma^2}\right) \tag{E.13}$$

and

$$\alpha_\nu = -c_3 B \frac{1}{\gamma^2}\int_{\gamma_{min}}^{\gamma_{max}} d\gamma\gamma^2 \frac{\partial}{\partial\gamma}\left[\frac{N\left(\gamma\right)}{\gamma^2}\right] F\left(\frac{\nu}{c_1 B\gamma^2}\right) \tag{E.14}$$

[1] Note: The two expressions 'hard photons' and 'high energy γ-rays' denote the same objects.
[2] Note: In general soft photons are (soft) x-ray photons or (hard) UV photons

with

$$F(x) = x \int_x^\infty K_{\frac{5}{3}}(x')dx' \tag{E.15}$$

$K_{\frac{5}{3}}(x)$ is the incomplete Bessel function of fractional order $\frac{5}{3}$and the constants are $c_1 = \frac{3e}{4\pi mc}$, $c_2 = \frac{\sqrt{3}e^3}{8\pi^2 mc^2}$ and $c_3 = \frac{\sqrt{3}e^3}{8\pi m^2 c^2}$. The electron density $N(\gamma)$ was shown in Equ. E.9.

Inverse Compton scattering

The emission coefficient of the inverse Compton scattering is obtained from the energy spectrum of the electrons Equ. E.9 as follows [Ino96]:

1. The ***emission coefficient***

$$j_\nu = \frac{h}{4\pi}\varepsilon q(\varepsilon) \tag{E.16}$$

and

$$\nu = \frac{m_e c^2}{h}\varepsilon \tag{E.17}$$

can be calculated from the

2. ***Differential hard photon production rate*** shown in Equ. E.18 (number of hard photons ε produced per energy interval per unit volume per unit time) which is a convolution of the electron distribution and the soft photon distribution (where the photon density is $n(\varepsilon_0)$, the soft photon energy is ε_0, the final photon energy is ε and the electron energy is γ , and everything is in units of electron masses)

$$q(\varepsilon) = \int d\varepsilon_0 n(\varepsilon_0) \int d\gamma N(\gamma)\ C(\varepsilon\,\gamma\,\varepsilon_0) \tag{E.18}$$

The probability for a soft photon to be up-scattered is called the

3. ***Compton kernel C*** and is given by:

$$C(\varepsilon,\gamma,\varepsilon_0) = \frac{2\pi r_e^2 c}{\gamma^2\varepsilon_0} \times \left[2\kappa\ln\kappa + (1+2\kappa)(1-\kappa) + \frac{(4\varepsilon_0\gamma\kappa)^2}{2(1+4\varepsilon_0\gamma\kappa)}(1-\kappa)\right] \tag{E.19}$$

where

$$\kappa = \frac{\varepsilon}{4\varepsilon_0\gamma(\gamma-\varepsilon)} \tag{E.20}$$

The ***allowed kinetic energy range*** for the up-scattered photon energy is

$$\varepsilon \le \varepsilon \le \gamma\frac{4\varepsilon_0\gamma}{(1+4\varepsilon_0\gamma)} \tag{E.21}$$

The ***hard photons can interact with the soft photons*** (and also with soft external thermal photons from the accretion disc) by creating electron-positron pairs, if their CM energy exceeds 1024 eV. This results in an ***attenuation*** of the hard photons and introduces an upper limit for the energy of the hard photons that can escape from the source. This gives a ***hard limit*** on the ***size*** of the emission region (***opacity condition***). For simplicity, we will neglect this effect here.

E.3 Error calculation of the correlation function

The empirical correlation function that has been used to find correlations between the x-ray flux and the γ-flux has been defined as:

$$\begin{aligned}
\rho(\Delta t) &= \frac{\sum_{i,k}\left(F^{\gamma}(t_k = t_i + \Delta t) - \langle F^{\gamma}\rangle\right)\left(F^{x}(t_i) - \langle F^{x}\rangle\right)}{\sqrt{\sum_i \left(F^{\gamma}(t_k = t_i + \Delta t) - \langle F^{\gamma}\rangle\right)^2 \sum_i \left(F^{x}(t_i) - \langle F^{x}\rangle\right)^2}} && \text{(E.22)}\\
&= \frac{\langle xy\rangle - \langle x\rangle\langle y\rangle}{\sigma_x \sigma_y} \\
&\quad with\, the\, shortcuts\ x, y: \\
x_i &= F^{\gamma}(t_k = t_i + \Delta t) && \text{(E.23)}\\
y_i &= F^{x}(t_i) && \text{(E.24)}\\
\delta x_i &= \sigma_{F^{\gamma}(t_k = t_i + \Delta t)} && \text{(E.25)}\\
\delta y_i &= \sigma_{F^{x}(t_i)} && \text{(E.26)}\\
\langle x\rangle &= \frac{1}{N}\sum_i x_i && \text{(E.27)}\\
\langle y\rangle &= \frac{1}{N}\sum y_i && \text{(E.28)}\\
\langle xy\rangle &= \frac{1}{N}\sum_i x_i y_i && \text{(E.29)}\\
\sigma_x^2 &= \frac{1}{N}\sum_i \left(x_i - \langle x\rangle\right)^2 && \text{(E.30)}\\
\sigma_y^2 & \quad \frac{1}{N}\sum_i \left(y_i - \langle y\rangle\right)^2 && \text{(E.31)}
\end{aligned}$$

$\rho = \rho(\Delta t)$ is the empirical correlation coefficient, $F^{\gamma}(t_k)$ is the γ-flux at time t_k, $F^{x}(t_i)$ is the x-ray flux at time t_i, Δt is the time lag between the two datasets and $\sigma_{F^{\gamma}}$ and $\sigma_{F^{x}}$ are the errors on the individual time bin measurement.

The error of the correlation has two components. One part $\sigma_{\rho,flux}$, comes directly from Gaussian error propagation of the errors on the fluxes [WitCom] and the second one $\sigma_{\rho,stat}$ is of statistical nature [Bro90, WitCom] of the correlation. Both of them have to be added. The uncertainty of the correlation coefficient which comes from the errors in the flux measurements are given in terms of the shortcuts above (for space reasons).

$$\begin{aligned}
\sigma_{\rho,tot}^2 &= \sigma_{\rho,flux}^2 + \sigma_{\rho,stat}^2 && \text{(E.32)}\\
\sigma_{\rho,flux}^2 &= \frac{1}{N}\sum_i \left(\frac{\left(y_i - \langle y\rangle\right) - \frac{\sigma_y}{\sigma_x}\left(x_i - \langle x\rangle\right)\rho}{\sigma_x\sigma_y}\right)^2 \delta x_i^2 + && \text{(E.33)}\\
&= \frac{1}{N}\sum_i \left(\frac{\left(x_i - \langle x\rangle\right) - \frac{\sigma_x}{\sigma_y}\left(y_i - \langle y\rangle\right)\rho}{\sigma_x\sigma_y}\right)^2 \delta y_i^2 \\
\sigma_{\rho,stat}^2 &= \frac{1-\rho^2}{N-2} && \text{(E.34)}
\end{aligned}$$

N is the number of samples that is being summed up. It is at the order of 80 (for the whole lightcurve in one day bins). The second term $\sigma_{\rho,stat}^2$ is in this case smaller than the first one but has to taken into account as well.

E.4 Re-binning and averaging of flux bins

For several reasons the flux bins must be re-binned or averaged over larger time periods (for correlation calculations or comparisons with other telescopes, for example see Fig. A.41) or flux level bins (for the hardness studies). The averaging has been done by weighting with the observation time of the corresponding run bin.

$$\langle F \rangle = \frac{\sum_{Bin} F_i T_i}{\sum_{Bin} T_i} \tag{E.35}$$

$$\sigma^2_{\langle F \rangle} = \frac{\sum_{Bin} \sigma^2_{F_i} T_i^2}{\left(\sum_{Bin} T_i\right)^2} = \frac{\sum_{Bin} \sigma^2_{F_i} T_i^2}{N_{eq} \sum_{Bin} T_i^2} \tag{E.36}$$

$$N_{eq} = \frac{\left(\sum_{Bin} T_i\right)^2}{\sum_{Bin} T_i^2} \tag{E.37}$$

F is understood as $F = \int (dF/dE)\, dE$. Here $\sigma^2_{\langle F \rangle}$ is variance of the mean and N_{eq} is the so-called equivalent number of events. It can be obtained by error propagation and it is needed to obtain the correct variance of the mean in the case of weighted averages.